

Communication

Defective PrO_x for Efficient Electrochemical NO₂[−]-to-NH₃ in a Wide Potential Range

Shunhan Jia ^{1,2} , Xingxing Tan ^{1,2}, Limin Wu ^{1,2}, Jiaqi Feng ¹, Libing Zhang ^{1,2}, Liang Xu ¹, Ruhan Wang ^{1,2}, Xiaofu Sun ^{1,2,*} and Buxing Han ^{1,2,3,*}

¹ Beijing National Laboratory for Molecular Sciences, CAS Key Laboratory of Colloid and Interface and Thermodynamics, CAS Research/Education Center for Excellence in Molecular Sciences, Institute of Chemistry, Chinese Academy of Sciences, Beijing 100190, China; jiashunhan@iccas.ac.cn (S.J.)

² School of Chemical Sciences, University of Chinese Academy of Sciences, Beijing 100049, China

³ Shanghai Key Laboratory of Green Chemistry and Chemical Processes, School of Chemistry and Molecular Engineering, East China Normal University, Shanghai 200062, China

* Correspondence: sunxiaofu@iccas.ac.cn (X.S.); hanbx@iccas.ac.cn (B.H.)

Abstract: Electrocatalytic reduction of nitrite (NO₂[−]) is a sustainable and carbon-neutral approach to producing green ammonia (NH₃). We herein report the first work on building defects on PrO_x for electrochemical NO₂[−] reduction to NH₃, and demonstrate a high NH₃ yield of 2870 μg h^{−1} cm^{−2} at the optimal potential of −0.7 V with a faradaic efficiency (FE) of 97.6% and excellent FEs of >94% at a wide given potential range (−0.5 to −0.8 V). The kinetic isotope effect (KIE) study suggested that the reaction involved promoted hydrogenation. Theoretical calculations clarified that there was an accelerated rate-determining step of NO₂[−] reduction on PrO_x. The results also indicated that PrO_x could be durable for long-term electrosynthesis and cycling tests.

Keywords: green chemistry; electrocatalysis; ammonia synthesis; rare earth; defect engineering



Citation: Jia, S.; Tan, X.; Wu, L.; Feng, J.; Zhang, L.; Xu, L.; Wang, R.; Sun, X.; Han, B. Defective PrO_x for Efficient Electrochemical NO₂[−]-to-NH₃ in a Wide Potential Range. *Chemistry* **2023**, *5*, 753–761. <https://doi.org/10.3390/chemistry5020053>

Academic Editors: José Antonio Odriozola and Hermenegildo García

Received: 22 February 2023

Revised: 26 March 2023

Accepted: 27 March 2023

Published: 29 March 2023



Copyright: © 2023 by the authors. Licensee MDPI, Basel, Switzerland. This article is an open access article distributed under the terms and conditions of the Creative Commons Attribution (CC BY) license (<https://creativecommons.org/licenses/by/4.0/>).

1. Introduction

Ammonia (NH₃) is not only one of the most essential chemicals, but also a promising high-density energy carrier contributing to carbon neutrality [1–6]. However, current NH₃ industrial production based on the traditional Haber–Bosch process suffers from harsh conditions and high CO₂ emissions [7–9]. Consequently, exploring a sustainable and carbon-neutral approach to green NH₃ is of great importance [10–12]. Recently, electrochemical N₂ reduction reaction (NRR) with H₂O as the proton source has caused worldwide concern as an alternating method for ambient NH₃ synthesis using clean energy [13,14]. Nevertheless, low N₂ solubility in aqueous electrolytes, hard N≡N bond (with an ultra-high bond energy of 941 kJ mol^{−1}) activation, and undesired hydrogen evolution reaction (HER) are becoming the main factors hindering the further application of NRR [15]. Compared with N₂, nitrite (NO₂[−]) has a higher solubility and lower dissociation energy of N=O bond (204 kJ mol^{−1}), coherently decreasing the thermodynamic limit of its conversion to NH₃ [16,17]. In addition, NO₂[−] is a widespread N-pollutant causing water pollution and a public health issue, and has also recently been reported as one of the main N₂ derivatives in eco-friendly plasmatic air oxidation [18–20]. Hence, electrocatalytic NO₂[−] reduction to NH₃ provides opportunities to remove NO₂[−] from contaminated water, utilization of renewable nitrogen sources, and production of green NH₃ through renewable energy-driven pathways.

Rare earth, the strategic source known as a modern industrial vitamin, was regarded as a key component in catalysts for many emerging reactions [21,22]. Its unique ground-state electronic configurations and unpaired 4f orbital electrons are expected to be promising electrocatalysts for NO₂[−] conversion. For instance, rare earth oxides such as CeO₂ could achieve an excellent performance for NH₃ electrosynthesis [23–25]. However, the reports

on rare earth-based catalysts are still very limited, and the catalytic activity needs to be improved further. Introducing defects to the surface of oxide catalysts was proved to be an efficient strategy to modulate the electron configuration of the catalytic sites and thus promote the formation and conversion of key intermediates during the reaction [26–29]. As a result, constructing defect structures could be a promising methodology to develop novel rare earth-based catalysts in the enhancement of NO_2^- reduction.

Herein, we have demonstrated the first work on building defects on praseodymium oxide (PrO_x) for electrochemical NO_2^- reduction to NH_3 . When tested using 0.01 M KNO_2 as the nitrogen source and 0.5 M K_2SO_4 as the supporting electrolyte, PrO_x could achieve a high NH_3 yield of $2870 \mu\text{g h}^{-1} \text{cm}^{-2}$ at -0.7 V, which is 8 times larger than the pristine Pr_6O_{11} . In addition, PrO_x could exhibit an excellent faradaic efficiency (FE) of $>94\%$ in a wide given potential range of -0.5 V to -0.8 V. The kinetic isotope effect (KIE) study indicates there is promoted hydrogenation during NO_2^- reduction on PrO_x . The NH_3 products were identified using isotope labelling. PrO_x also showed robust durability for long-term bulk electrosynthesis and cycling tests.

2. Results and Discussion

The process of preparing defective PrO_x catalysts is illustrated in Figure 1A. The intermediate products obtained from the hydrothermal method were proven to be $\text{Pr}(\text{OH})_3$ nanorods by X-ray diffraction (XRD, JCPDS No. 83-2304) patterns, scanning electron microscopy (SEM), and transmission electron microscopy (TEM) in Figures S1–S4, which could transfer to Pr_6O_{11} through calcining in air [30]. Thermal treatment of Pr_6O_{11} in an H_2 atmosphere at different temperatures (300°C , 500°C , and 700°C) was utilized to construct oxygen vacancies (V_o) on its surface. The obtained samples were denoted as $\text{PrO}_x\text{-T}$ ($T = 300, 500, \text{ and } 700$). The XRD patterns of Pr_6O_{11} and $\text{PrO}_x\text{-500}$ are exhibited in Figure 1B. Similar peaks presented by Pr_6O_{11} and $\text{PrO}_x\text{-500}$ at $27.7, 32.1, 46.1, 54.6^\circ$ are well indexed to the (111), (200), (220), and (311) crystallographic planes of Pr_6O_{11} (JCPDS No. 42-1121). Very little Pr_2O_3 phase (JCPDS No. 74-1146) was observed. The gradual color change was found from the optical photograph (Figure 1B inset and Figure S5) from Pr_6O_{11} to PrO_x powders, which was characteristic of Pr^{3+} and indicated the increase of Pr^{3+} with the increasing temperature of PrO_x preparation [31]. The results of XRD as well as SEM and low-resolution TEM images shown in Figure 1C and Figures S6–S8, indicated that the introduction of defects could not result in a significant change of crystal phase, morphology, and particle size of ca. 200 nm. High-resolution TEM (HR-TEM) images in Figure 1D and Figure S9 revealed that $\text{PrO}_x\text{-500}$ posed distinct lattice fringes and a lattice spacing of 0.326 nm, which could be consistent with the cubic fluorite structure of the Pr_6O_{11} (111) plane. In addition, $\text{PrO}_x\text{-500}$ exhibited disrupted fringes due to the presence of dot defects which was not observed in Pr_6O_{11} samples (Figure S10), thereby confirming the existence of defects introduced by the H_2 treatment. Figure 1E displays the energy-dispersive X-ray (EDX) elemental mapping images of $\text{PrO}_x\text{-500}$, suggesting there was uniform distribution of Pr and O elements.

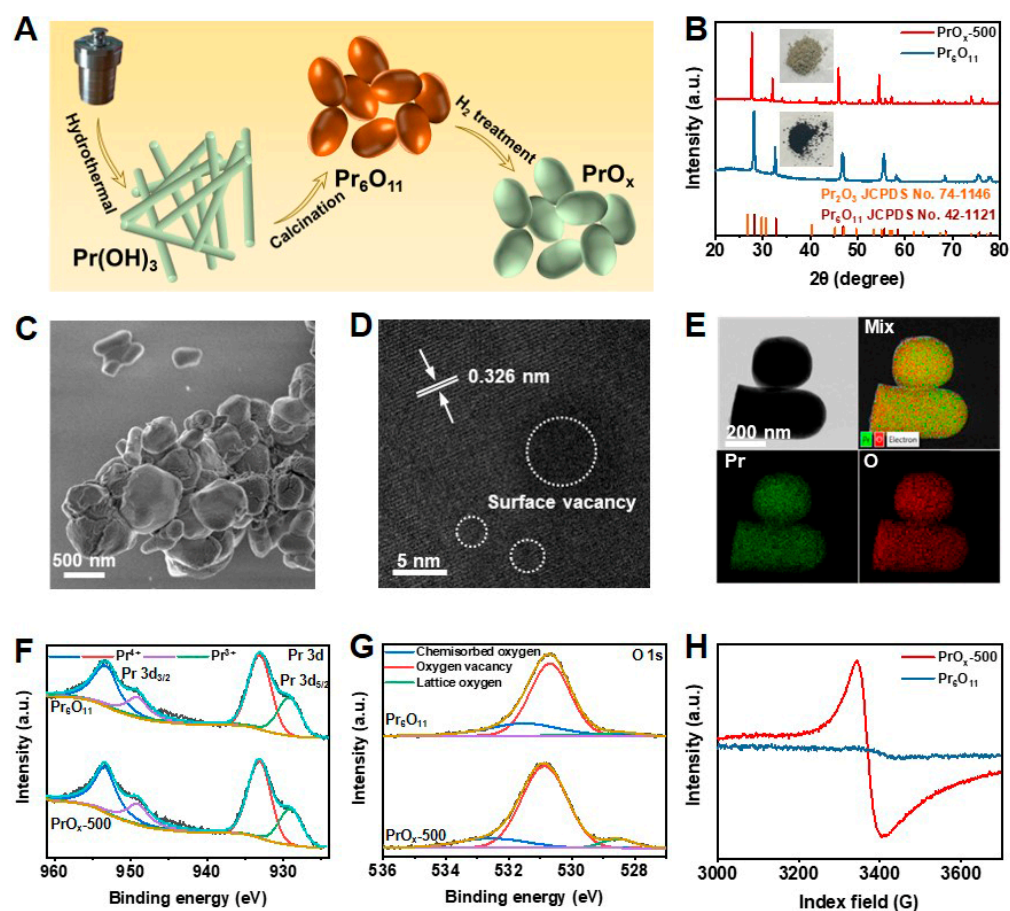


Figure 1. (A) Schematic illustration of the synthesis of PrO_x electrocatalyst. (B) XRD patterns and optical photographs (inset) of Pr_6O_{11} and PrO_x -500. (C) SEM image of PrO_x -500. (D) HR-TEM image and (E) corresponding EDX mapping images of PrO_x -500. XPS spectra of Pr_6O_{11} and PrO_x -500 in the regions of (F) Pr 3d and (G) O 1s. (H) EPR curves of Pr_6O_{11} and PrO_x -500.

Further analysis of the PrO_x surface was performed using X-ray photoelectron spectroscopy (XPS, AXIS ULTRA DLD, UK). The Pr 3d spectra in Figure 1F and Figure S11 were observed in the PrO_x -500 sample, with peaks at 953.1 eV (Pr 3d_{3/2}) and 933.1 eV (Pr 3d_{5/2}) being attributed to Pr^{4+} and peaks at 949.1 eV (Pr 3d_{3/2}) and 929.2 eV (Pr 3d_{5/2}) being assigned to Pr^{3+} [32,33]. As the temperature increased, the intensity of the Pr^{3+} peaks increased, indicating that more Pr^{4+} was reduced to Pr^{3+} . The O 1s spectra in Figure 1G and Figure S12 indicated the presence of different chemical environments for oxygen atoms in the PrO_x catalysts. The concentration of V_o increased with the increasing calcination temperature. The peaks at 531.5, 530.7, and 528.3 eV corresponded to chemisorbed oxygen, oxygen deficiency, and lattice oxygen, respectively [34–36]. As the temperature increased, the peak of oxygen vacancy was found to increase due to more V_o on the surface of PrO_x -500 compared with Pr_6O_{11} . The slight shifts of Pr 3d and O 1s peaks between Pr_6O_{11} and PrO_x samples were also attributed to the introduced defects. Electron paramagnetic resonance (EPR) spectra were used to confirm the presence of V_o in Pr_6O_{11} and PrO_x catalysts (Figure 1H). Compared with Pr_6O_{11} , PrO_x had a distinct EPR signal of V_o at $g = 2.004$, demonstrating again the successful preparation of PrO_x with V_o [31–37].

The electrochemical performance of PrO_x -500 for NH_3 synthesis was evaluated in 0.5 M K_2SO_4 aqueous solution with 0.01 M KNO_2 saturated by Ar, utilizing an H-type cell with a three-electrode configuration (Figure S13). All potentials reported in this paper were converted to the relative hydrogens electrode (RHE). The performances reported in this paper are verified by three repeated experiments, and the average results with error bars are given. A catalyst ink of PrO_x -500 powder was prepared and loaded on a carbon paper

evenly (1 mg cm^{-2}), which served as the working electrode. As presented in Figure 2A, the electrochemical catalytic activity of PrO_x-500 for NO₂[−] reduction to NH₃ was firstly investigated using the linear scanning voltammetry (LSV) curves (scan rate = 10 mV s^{-1}). Adding 0.01 M KNO₂ promoted the current density (*j*) remarkably, indicating there was excellent activity of NO₂[−] reduction over PrO_x-500 in neutral media. To investigate the optimal efficiency of NH₃ production, chronoamperometry tests were carried out by applying various potentials ranging from -0.4 to -0.9 V. As shown in Figure 2B, these chronoamperometry curves remained stable during electrochemical tests for 3600 s. The corresponding UV-vis spectra showed that the peak of absorption curves increased with the applied potential, meaning there was an increase in the NH₃ yield with growing potential (Figure 2C). The NH₃ yield and FE calculated from calibration curves in Figure S14 are presented in Figure 2D. PrO_x-500 exhibited the highest FE of 97.6% at -0.7 V with a NH₃ yield of $2870 \text{ } \mu\text{g h}^{-1} \text{ cm}^{-2}$. In addition, PrO_x-500 had an ideal performance with an FE of >94% from the range of applied potential from -0.5 to -0.8 V, which is essential for further application. Since -0.7 V was chosen as the optimal potential for NH₃ production, we further studied different Pr-based catalysts on -0.7 V. The results in Figure 2E indicate that Pr₆O₁₁, PrO_x-300, and PrO_x-700 exhibited lower NH₃ yields (372 , 1643 , and $1387 \text{ } \mu\text{g h}^{-1} \text{ cm}^{-2}$) and poor FEs (19.7%, 67.8%, and 58.2%), implying that the construction of defects under optimal temperature is a useful strategy to boost NO₂[−] reduction reaction for NH₃ electrosynthesis. Further experiments were conducted to clarify the acceleration of the kinetics process during the NO₂[−] reduction by examining the KIE of H/D (H₂O/D₂O) over the Pr₆O₁₁ and PrO_x-500 catalysts. The KIE values, which serve as a descriptor of proton transfer rate, were calculated and compared in Figure 2F. The results showed a significant decrease in KIE value from 1.58 in the PrO_x-500 sample to 1.24 in the PrO_x-500 catalyst, indicating there was a faster rate of hydrogenation kinetics [38–40]. Additionally, the onset potential of the Pr₆O₁₁ and PrO_x 500 samples depicted in Figure 2F (inset) suggested that their performance was enhanced in H₂O solvent as compared to D₂O solvent, which is consistent with the variation in NH₃ yield obtained using different catalysts and solvents. To eliminate the influence of other nitrogen sources, control experiments were performed. The results of these experiments, as presented in Figure 3A, indicated that our electrodes, electrolyte, and reagents were not contaminated by N-impurities, as there was an absence of NH₃ production in the cathode solution after electrolysis at the open circuit potential (OCP) with a blank electrolyte. The NH₃ production of PrO_x-500 was further evaluated by alternately conducting experiments in electrolytes with and without NO₂[−] for three cycles at -0.7 V (Figure 3B). The results showed that NH₃ was only detected in electrolytes containing NO₂[−]. Next, ¹⁵N isotope labelling was performed using ¹⁵NO₂[−] as an additive electrolyte. Figure 3C showed two peaks of ¹⁵NH₄⁺ and three peaks of ¹⁴NH₄⁺ in the corresponding ¹H Nuclear magnetic resonance (NMR) spectra (signals of standard samples were shown in Figure S15), obtained from experiments with ¹⁵NO₂[−] and ¹⁴NO₂[−] as additive electrolytes, further confirming that the NH₃ came from the reduction of NO₂[−]. The stability of electrocatalysts is critical for industrial applications because it determines the longevity and efficiency of the electrochemical reactions [41]. To assess the remarkable catalytic stability of PrO_x-500, we performed cycling experiments using the same working electrode and refreshed the electrolyte for each cycle. The results showed that the NH₃ yields and FEs for the ten cycles remained stable with negligible fluctuations. In addition, the similarity in color (Figure S16), XRD patterns (Figure S17), SEM images (Figure S18), TEM images (Figure S19), EDS elemental mapping images (Figure S20), XPS spectra (Figures S21 and S22), and LSV curves (Figure S23) of PrO_x-500, both prior to and after extended electrolysis, further supports the excellent electrochemical and structural stability of PrO_x-500 as a catalyst in the reduction of NO₂[−] for the synthesis of NH₃.

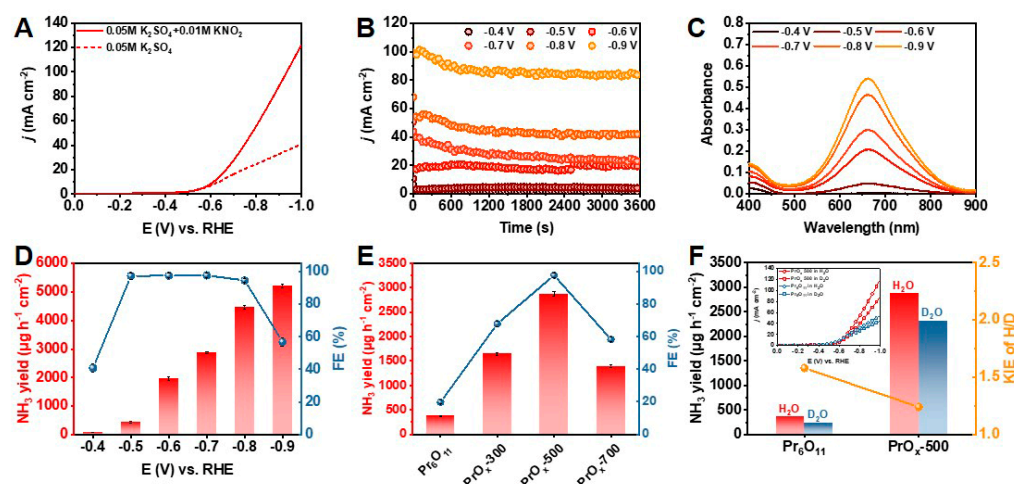


Figure 2. (A) LSV curves of PrO_x-500 in 0.5 M K₂SO₄ aqueous solution in the presence and absence of 0.01 M KNO₂. (B) Chronoamperometry curves of NO₂[−] reduction from −0.4 V to −0.9 V over PrO_x-500 catalyst. (C) Corresponding UV-vis spectra of PrO_x-500 catalyzed NO₂[−] reduction. (D) Potential-dependent NH₃ yields and FE of PrO_x-500. (E) Comparison of the performance of various Pr-based catalysts. (F) KIE study of H/D over Pr₆O₁₁ and PrO_x-500 and LSV curves (inset) of Pr₆O₁₁ and PrO_x-500 in H₂O and D₂O solvents.

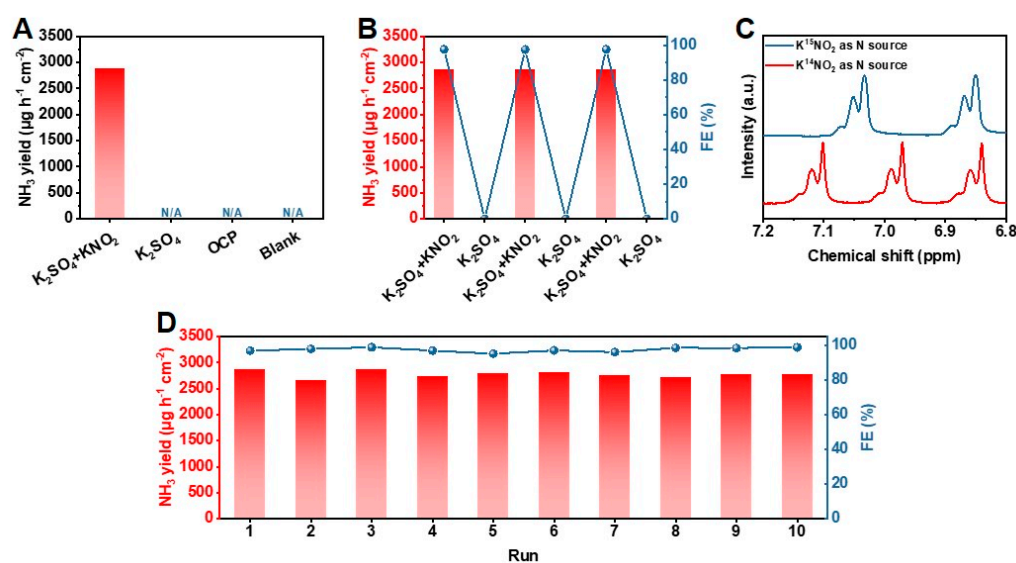


Figure 3. (A) NH₃ yields of PrO_x-500 for NO₂[−] reduction at various conditions. (B) NH₃ yields and FE of NO₂[−] reduction on PrO_x-500 during the alternating cycling test between 0.5 M K₂SO₄ with/without additional 0.01 M KNO₂. (C) ¹H NMR spectra of NH₃ products in the electrolytes after the reduction of K¹⁴NO₂ and K¹⁵NO₂ at −0.7 V for 3600 s. (D) NH₃ yields and FE of PrO_x-500 during consecutive recycling tests.

A density functional theory (DFT) study was then carried out to investigate the reaction pathways of NO₂[−] reduction on Pr-based catalysts with different defects and thus modified electronic structure. The (111) facet was found to be the main plane in Pr₆O₁₁ and PrO_x samples according to XRD patterns and HR-TEM images shown in Figure 1B and 1D. The catalyst models of PrO_x(111) were thus built by constructing V_o on the perfect Pr₆O₁₁(111) facet. Figure 4A presented the reaction-free energy levels of various intermediates for NO₂[−] reduction on PrO_x and Pr₆O₁₁, revealing that the rate-determining step (RDS) on the PrO_x and Pr₆O₁₁ surface was *NOH plus H to generate *N. Additionally, the corresponding structures of NO₂[−] reduction intermediates are illustrated in Figure 4B,C. On the surface of PrO_x, the coordination number of Pr near the defect was lower, thus increasing the

adsorption capacity of *N , and lowering the energy barrier of the PDS. Hence, the free energy of the final RDS on PrO_x is reduced compared to that on the perfect Pr_6O_{11} surface. Hence, constructing defects on PrO_x catalysts could significantly accelerate the RDS, leading to the better performance of electrochemical NO_2^- reduction.

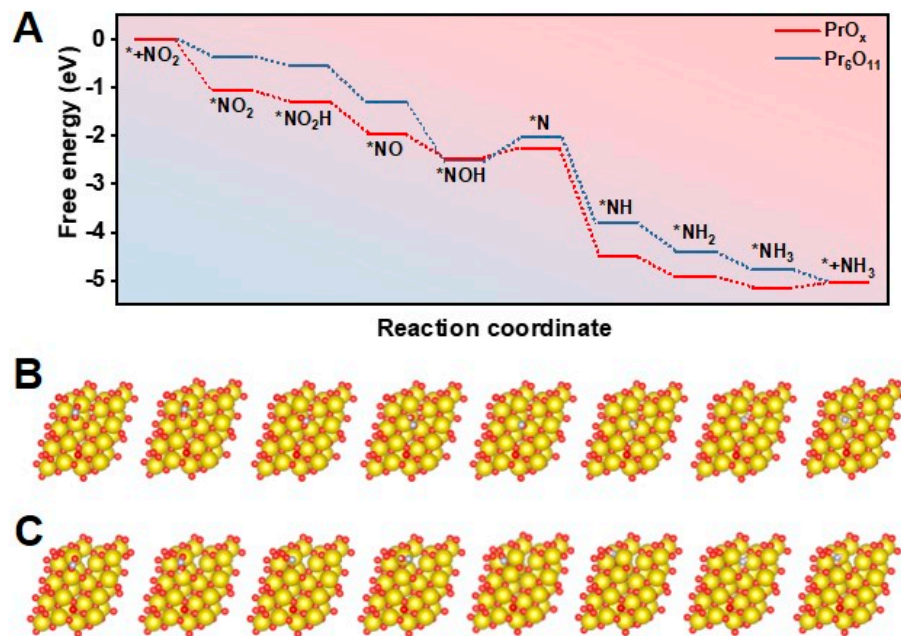


Figure 4. (A) Free energy of various intermediates generated during NO_2^- reduction on $PrO_x(111)$ and $Pr_6O_{11}(111)$. Atomic configurations of the intermediates on (B) $PrO_x(111)$ and (C) $Pr_6O_{11}(111)$ during the electrochemical progress (Pr: gold, O: red, N: purple, and H: pink).

3. Conclusions

In summary, this work has demonstrated the highly efficient electrochemical reduction of NO_2^- to NH_3 utilizing PrO_x catalysts with defects. Electrocatalysis tests showed a high yield of $2870 \mu g h^{-1} cm^{-2}$ at an optimal potential of $-0.7 V$ and FE of $>94\%$ in a wide applied potential range. A KIE study confirmed the promotion of hydrogenation during the reduction process, and the products were identified using isotope labelling. Additionally, PrO_x demonstrated robust durability for long-term electrosynthesis and cycling tests. DFT calculations demonstrated that PrO_x could accelerate the RDS of NO_2^- reduction, resulting in the enhanced performance of NH_3 production. The work opens up new avenues for the development of ambient, efficient, and sustainable NH_3 synthesis processes and lays a foundation for the development of next-generation electrochemical systems for environmental protection, energy conversion, and chemical manufacturing.

Supplementary Materials: The following supporting information can be downloaded at: <https://www.mdpi.com/article/10.3390/chemistry5020053/s1>, Figure S1. Optical photograph of $Pr(OH)_3$ after hydrothermal treatment, Figure S2. XRD pattern of $Pr(OH)_3$ obtained from hydrothermal method, Figure S3. SEM images of synthesized $Pr(OH)_3$ nanorods, Figure S4. TEM image of $Pr(OH)_3$ nanorods, Figure S5. Optical photograph of (A) PrO_x -300 and (B) PrO_x -700 samples, XRD patterns of (A) PrO_x -300 and (B) PrO_x -700, Figure S7. SEM images of the as-synthesized (A) Pr_6O_{11} , (B) PrO_x -300, and (C) PrO_x -700 samples, Figure S8. TEM images of the as-synthesized (A) Pr_6O_{11} , (B) PrO_x -300, and (C) PrO_x -700, Figure S9. Well-resolved lattice fringe of PrO_x -500 in Figure 1D, Figure S10. HR-TEM image of Pr_6O_{11} , Figure S11. XPS curves of Pr 3d orbital of PrO_x -300 and PrO_x -700 surface, Figure S12. XPS curves of O 1s orbital of PrO_x -300 and PrO_x -700 surface, Figure S13. Illustration of H-cell used in this study, Figure S14. UV-vis absorption curves of indophenol assays kept with samples with different $[NH_4^+]$ for at least 2 h at $25^\circ C$. (b) Calibration curve to estimate unknown $[NH_4^+]$, Figure S15. 1H NMR spectra of $^{15}NH_4^+$ and $^{14}NH_4^+$ standard samples, Figure S16. Optical photograph of working electrodes loading with PrO_x -500 catalysts before and after reactions,

Figure S17. XRD pattern of PrO_x-500 after electrolysis, Figure S18. SEM image of PrO_x-500 after electrolysis, Figure S19. TEM image of PrO_x-500 after electrolysis, Figure S20. EDX mappings of PrO_x-500 after electrolysis, Figure S21. XPS curves of Pr 3d orbital of PrO_x-500 surface after reduction, Figure S22. XPS curves of O 1s orbital of PrO_x-500 surface after reduction, Figure S23. LSV curves of PrO_x-500 before and after reduction. References [30,42–45] are cited in the supplementary materials.

Author Contributions: Conceptualization, S.J., X.S. and B.H.; methodology, S.J., X.S. and B.H.; formal analysis, X.T., L.W., J.F., L.Z., L.X. and R.W.; writing—original draft preparation, S.J.; writing—review and editing, X.S. and B.H.; supervision, X.S. and B.H. All authors have read and agreed to the published version of the manuscript.

Funding: This research was supported by National Natural Science Foundation of China (22002172, 22121002 and 22203099) and China Postdoctoral Science Foundation (2022M713200).

Data Availability Statement: The data presented in this study are available on request from the corresponding authors (Prof. Xiaofu Sun and Prof. Buxing Han).

Acknowledgments: The authors thank the staff at Centre for Physicochemical Analysis & Measurement of ICCAS for material characterizations.

Conflicts of Interest: The authors declare no conflict of interest.

References

1. Erisman, J.W.; Sutton, M.A.; Galloway, J.; Klimont, Z.; Winiwarter, W. How a century of ammonia synthesis changed the world. *Nat. Geosci.* **2008**, *1*, 636–639. [[CrossRef](#)]
2. MacFarlane, D.R.; Cherepanov, P.V.; Choi, J.; Suryanto, B.H.R.; Hodgetts, R.Y.; Bakker, J.M.; Ferrero Vallana, F.M.; Simonov, A.N. A Roadmap to the Ammonia Economy. *Joule* **2020**, *4*, 1186–1205. [[CrossRef](#)]
3. Wang, B.; Ni, M.; Jiao, K. Green ammonia as a fuel. *Sci. Bull.* **2022**, *67*, 1530–1534. [[CrossRef](#)]
4. He, M.; Zhang, K.; Guan, Y.; Sun, Y.; Han, B. Green carbon science: Fundamental aspects. *Natl. Sci. Rev.* **2023**, nwad046. [[CrossRef](#)]
5. He, M.; Sun, Y.; Han, B. Green Carbon Science: Scientific Basis for Integrating Carbon Resource Processing, Utilization, and Recycling. *Angew. Chem. Int. Ed.* **2013**, *52*, 9620–9633. [[CrossRef](#)]
6. He, M.; Sun, Y.; Han, B. Green Carbon Science: Efficient Carbon Resource Processing, Utilization, and Recycling towards Carbon Neutrality. *Angew. Chem. Int. Ed.* **2022**, *61*, e202112835. [[CrossRef](#)]
7. Chen, J.G.; Crooks, R.M.; Seefeldt, L.C.; Bren, K.L.; Bullock, R.M.; Darensbourg, M.Y.; Holland, P.L.; Hoffman, B.; Janik, M.J.; Jones, A.K.; et al. Beyond fossil fuel-driven nitrogen transformations. *Science* **2018**, *360*, eaar6611. [[CrossRef](#)] [[PubMed](#)]
8. Xia, R.; Overa, S.; Jiao, F. Emerging Electrochemical Processes to Decarbonize the Chemical Industry. *JACS Au* **2022**, *2*, 1054–1070. [[CrossRef](#)]
9. Song, X.; Jia, S.; Xu, L.; Feng, J.; He, L.; Sun, X.; Han, B. Towards sustainable CO₂ electrochemical transformation via coupling design strategy. *Mater. Today Sustain.* **2022**, *19*, 100179. [[CrossRef](#)]
10. Foster, S.L.; Bakovic, S.I.P.; Duda, R.D.; Maheshwari, S.; Milton, R.D.; Minter, S.D.; Janik, M.J.; Renner, J.N.; Greenlee, L.F. Catalysts for nitrogen reduction to ammonia. *Nat. Catal.* **2018**, *1*, 490–500. [[CrossRef](#)]
11. Wang, F.; Harindintwali, J.D.; Yuan, Z.; Wang, M.; Wang, F.; Li, S.; Yin, Z.; Huang, L.; Fu, Y.; Li, L.; et al. Technologies and perspectives for achieving carbon neutrality. *Innovation* **2021**, *2*, 100180. [[CrossRef](#)] [[PubMed](#)]
12. Zhang, X.; Wang, Y.; Wang, Y.; Guo, Y.; Xie, X.; Yu, Y.; Zhang, B. Recent advances in electrocatalytic nitrite reduction. *Chem. Commun.* **2022**, *58*, 2777–2787. [[CrossRef](#)] [[PubMed](#)]
13. Wu, L.; Guo, W.; Sun, X.; Han, B. Rational design of nanocatalysts for ambient ammonia electrosynthesis. *Pure Appl. Chem.* **2021**, *93*, 777–797. [[CrossRef](#)]
14. Jia, S.; Wu, L.; Xu, L.; Sun, X.; Han, B. Multicomponent catalyst design for CO₂/N₂/NO_x electroreduction. *Ind. Chem. Mater.* **2023**, *1*, 93–105. [[CrossRef](#)]
15. Iriawan, H.; Andersen, S.Z.; Zhang, X.; Comer, B.M.; Barrio, J.; Chen, P.; Medford, A.J.; Stephens, I.E.L.; Chorkendorff, I.; Shao-Horn, Y. Methods for nitrogen activation by reduction and oxidation. *Nat. Rev. Methods Prim.* **2021**, *1*, 56. [[CrossRef](#)]
16. Stirling, A.; Papai, I.; Mink, J.; Salahub, D.R. Density functional study of nitrogen oxides. *J. Chem. Phys.* **1994**, *100*, 2910–2923. [[CrossRef](#)]
17. Wu, L.; Zhang, L.; Liu, S.; Feng, J.; Xu, L.; Tan, X.; Ma, X.; Sun, X. Promoting ambient ammonia electrosynthesis on modulated Cu^{δ+} catalysts by B-doping. *J. Mater. Chem. A* **2023**, *11*, 5520–5526. [[CrossRef](#)]
18. Galloway, J.N.; Townsend, A.R.; Erisman, J.W.; Bekunda, M.; Cai, Z.; Freney, J.R.; Martinelli, L.A.; Seitzinger, S.P.; Sutton, M.A. Transformation of the Nitrogen Cycle: Recent Trends, Questions, and Potential Solutions. *Science* **2008**, *320*, 889–892. [[CrossRef](#)]
19. Li, L.; Tang, C.; Cui, X.; Zheng, Y.; Wang, X.; Xu, H.; Zhang, S.; Shao, T.; Davey, K.; Qiao, S.-Z. Efficient Nitrogen Fixation to Ammonia through Integration of Plasma Oxidation with Electrocatalytic Reduction. *Angew. Chem. Int. Ed.* **2021**, *60*, 14131–14137. [[CrossRef](#)]

20. Ren, Y.; Yu, C.; Wang, L.; Tan, X.; Wang, Z.; Wei, Q.; Zhang, Y.; Qiu, J. Microscopic-Level Insights into the Mechanism of Enhanced NH_3 Synthesis in Plasma-Enabled Cascade N_2 Oxidation–Electroreduction System. *J. Am. Chem. Soc.* **2022**, *144*, 10193–10200. [[CrossRef](#)]
21. Xu, J.; Chen, X.; Xu, Y.; Du, Y.; Yan, C. Ultrathin 2D Rare-Earth Nanomaterials: Compositions, Syntheses, and Applications. *Adv. Mater.* **2020**, *32*, 1806461. [[CrossRef](#)] [[PubMed](#)]
22. Zhang, S.; Saji, S.E.; Yin, Z.; Zhang, H.; Du, Y.; Yan, C.-H. Rare-Earth Incorporated Alloy Catalysts: Synthesis, Properties, and Applications. *Adv. Mater.* **2021**, *33*, 2005988. [[CrossRef](#)] [[PubMed](#)]
23. Li, Z.; Deng, Z.; Ouyang, L.; Fan, X.; Zhang, L.; Sun, S.; Liu, Q.; Alshehri, A.A.; Luo, Y.; Kong, Q.; et al. CeO_2 nanoparticles with oxygen vacancies decorated N-doped carbon nanorods: A highly efficient catalyst for nitrate electroreduction to ammonia. *Nano Res.* **2022**, *15*, 8914–8921. [[CrossRef](#)]
24. Liu, Y.; Li, C.; Guan, L.; Li, K.; Lin, Y. Oxygen Vacancy Regulation Strategy Promotes Electrocatalytic Nitrogen Fixation by Doping Bi into Ce-MOF-Derived CeO_2 Nanorods. *J. Phys. Chem. C* **2020**, *124*, 18003–18009. [[CrossRef](#)]
25. Liu, G.; Cui, Z.; Han, M.; Zhang, S.; Zhao, C.; Chen, C.; Wang, G.; Zhang, H. Ambient Electrosynthesis of Ammonia on a Core–Shell-Structured Au/CeO₂ Catalyst: Contribution of Oxygen Vacancies in CeO_2 . *Chem. Eur. J.* **2019**, *25*, 5904–5911. [[CrossRef](#)] [[PubMed](#)]
26. Yan, D.; Li, H.; Chen, C.; Zou, Y.; Wang, S. Defect Engineering Strategies for Nitrogen Reduction Reactions under Ambient Conditions. *Small Methods* **2019**, *3*, 1800331. [[CrossRef](#)]
27. Yang, C.; Lu, Y.; Zhang, L.; Kong, Z.; Yang, T.; Tao, L.; Zou, Y.; Wang, S. Defect Engineering on CeO_2 -Based Catalysts for Heterogeneous Catalytic Applications. *Small Struct.* **2021**, *2*, 2100058. [[CrossRef](#)]
28. Xu, L.; Feng, J.; Wu, L.; Song, X.; Tan, X.; Zhang, L.; Ma, X.; Jia, S.; Du, J.; Chen, A.; et al. Identifying the optimal oxidation state of Cu for electrocatalytic reduction of CO_2 to C_{2+} products. *Green Chem.* **2023**, *25*, 1326–1331. [[CrossRef](#)]
29. Zhang, L.; Feng, J.; Liu, S.; Tan, X.; Wu, L.; Jia, S.; Xu, L.; Ma, X.; Song, X.; Ma, J.; et al. Atomically Dispersed Ni–Cu Catalysts for pH-Universal CO_2 Electroreduction. *Adv. Mater.* **2023**, 2209590. [[CrossRef](#)]
30. Huang, P.X.; Wu, F.; Zhu, B.L.; Li, G.R.; Wang, Y.L.; Gao, X.P.; Zhu, H.Y.; Yan, T.Y.; Huang, W.P.; Zhang, S.M.; et al. Praseodymium Hydroxide and Oxide Nanorods and Au/ Pr_6O_{11} Nanorod Catalysts for CO Oxidation. *J. Phys. Chem. B* **2006**, *110*, 1614–1620. [[CrossRef](#)]
31. Su, L.; Zhang, Y.; Zhan, X.; Zhang, L.; Zhao, Y.; Zhu, X.; Wu, H.; Chen, H.; Shen, C.; Wang, L. Pr_6O_{11} : Temperature-Dependent Oxygen Vacancy Regulation and Catalytic Performance for Lithium–Oxygen Batteries. *ACS Appl. Mater. Interfaces* **2022**, *14*, 40975–40984. [[CrossRef](#)]
32. Tankov, I.; Arishtirova, K.; Bueno, J.M.C.; Damyanova, S. Surface and structural features of Pt/ PrO_2 – Al_2O_3 catalysts for dry methane reforming. *App. Catal. A Gen.* **2014**, *474*, 135–148. [[CrossRef](#)]
33. Guo, M.; Lu, J.; Wu, Y.; Wang, Y.; Luo, M. UV and Visible Raman Studies of Oxygen Vacancies in Rare-Earth-Doped Ceria. *Langmuir* **2011**, *27*, 3872–3877. [[CrossRef](#)]
34. Sanivarapu, S.R.; Lawrence, J.B.; Sreedhar, G. Role of Surface Oxygen Vacancies and Lanthanide Contraction Phenomenon of $\text{Ln}(\text{OH})_3$ (Ln = La, Pr, and Nd) in Sulfide-Mediated Photoelectrochemical Water Splitting. *ACS Omega* **2018**, *3*, 6267–6278. [[CrossRef](#)] [[PubMed](#)]
35. Lei, F.; Sun, Y.; Liu, K.; Gao, S.; Liang, L.; Pan, B.; Xie, Y. Oxygen Vacancies Confined in Ultrathin Indium Oxide Porous Sheets for Promoted Visible-Light Water Splitting. *J. Am. Chem. Soc.* **2014**, *136*, 6826–6829. [[CrossRef](#)] [[PubMed](#)]
36. Wang, C.; Ren, D.; Harle, G.; Qin, Q.; Guo, L.; Zheng, T.; Yin, X.; Du, J.; Zhao, Y. Ammonia removal in selective catalytic oxidation: Influence of catalyst structure on the nitrogen selectivity. *J. Hazard. Mater.* **2021**, *416*, 125782. [[CrossRef](#)] [[PubMed](#)]
37. Guo, W.; Liu, S.; Tan, X.; Wu, R.; Yan, X.; Chen, C.; Zhu, Q.; Zheng, L.; Ma, J.; Zhang, J.; et al. Highly Efficient CO_2 Electroreduction to Methanol through Atomically Dispersed Sn Coupled with Defective CuO Catalysts. *Angew. Chem. Int. Ed.* **2021**, *60*, 21979–21987. [[CrossRef](#)]
38. Yang, Y.; Agarwal, R.G.; Hutchison, P.; Rizo, R.; Soudackov, A.V.; Lu, X.; Herrero, E.; Feliu, J.M.; Hammes-Schiffer, S.; Mayer, J.M.; et al. Inverse kinetic isotope effects in the oxygen reduction reaction at platinum single crystals. *Nat. Chem.* **2022**, *15*, 271–277. [[CrossRef](#)] [[PubMed](#)]
39. Fan, K.; Xie, W.; Li, J.; Sun, Y.; Xu, P.; Tang, Y.; Li, Z.; Shao, M. Active hydrogen boosts electrochemical nitrate reduction to ammonia. *Nat. Commun.* **2022**, *13*, 7958. [[CrossRef](#)]
40. Kong, Y.; Li, Y.; Sang, X.; Yang, B.; Li, Z.; Zheng, S.; Zhang, Q.; Yao, S.; Yang, X.; Lei, L.; et al. Atomically Dispersed Zinc(I) Active Sites to Accelerate Nitrogen Reduction Kinetics for Ammonia Electrosynthesis. *Adv. Mater.* **2022**, *34*, 2103548. [[CrossRef](#)]
41. Jia, S.; Ma, X.; Sun, X.; Han, B. Electrochemical Transformation of CO_2 to Value-Added Chemicals and Fuels. *CCS Chem.* **2022**, *4*, 3213–3229. [[CrossRef](#)]
42. Wu, Y.; Jiang, Z.; Lin, Z.; Liang, Y.; Wang, H. Direct electrosynthesis of methylamine from carbon dioxide and nitrate. *Nat. Sustain.* **2021**, *4*, 725–730. [[CrossRef](#)]
43. Perdew, J.P.; Burke, K.; Ernzerhof, M. Generalized Gradient Approximation Made Simple. *Phys. Rev. Lett.* **1996**, *77*, 3865–3868. [[CrossRef](#)] [[PubMed](#)]

44. Kresse, G.; Furthmuller, J. Efficient Iterative Schemes for Ab Initio Total-Energy Calculations Using a Plane-Wave Basis Set. *Phys. Rev. B Condens. Matter.* **1996**, *54*, 11169–11186. [[CrossRef](#)] [[PubMed](#)]
45. Grimme, S.; Antony, J.; Ehrlich, S.; Krieg, H. A Consistent and Accurate Ab Initio Parametrization of Density Functional Dispersion Correction (DFT-D) for the 94 Elements H-Pu. *J. Chem. Phys.* **2010**, *132*, 154104. [[CrossRef](#)]

Disclaimer/Publisher's Note: The statements, opinions and data contained in all publications are solely those of the individual author(s) and contributor(s) and not of MDPI and/or the editor(s). MDPI and/or the editor(s) disclaim responsibility for any injury to people or property resulting from any ideas, methods, instructions or products referred to in the content.